Article

Dynamical Change of Valence States and Structure in NiCu₃ Nanoparticles during Redox Cycling

Alexandre C. Foucher, Nicholas Marcella, Jennifer D. Lee, Ryan Tappero, Christopher B. Murray, Anatoly I. Frenkel, and Eric A. Stach*

Cite This: *J. Phys. Chem. C* 2022, 126, 1991−2002

Read Online

ACCESS | Metrics & More | Article Recommendations | Supporting Information

ABSTRACT: Alloyed materials are promising candidates to improve catalytic processes. Ni−Cu nanoparticles are used for various reactions, including processes with biomass-derived components. However, dynamical restructuring effects alter the catalytic properties and can deactivate the sample. To understand these structural modifications, a multimodal investigation of NiCu₃/C was performed to determine compositional and morphological changes during a redox cycle to simulate reduction and oxidation of the catalyst during reaction. We exploit a novel correlative, multimodal approach that combines in situ X-ray absorption spectroscopy (XAS) and in situ scanning transmission electron microscopy and electron energy-loss spectroscopy (STEM-EELS) to describe changes that occur in the sample in

realistic conditions. In the fresh sample, there are two morphologies present: core−shell and hollow. Segregation of Cu was observed in both types of particles after synthesis, with Cu being more oxidized in the hollow structures. Upon reduction for 2 h under H₂ at 400 °C, the Cu was reduced, although segregation of Cu and Ni was still observed. Subsequent exposure to O₂ at 400 °C led to a strong reoxidation of Cu with the formation of hollow particles with compositional heterogeneities. The oxidation of metals and segregation phenomena can be related to known catalytic properties of NiCu₃/C particles, especially regarding the hydrodeoxygenation of 5-hydroxymethylfurfural to 2,5-dimethylfuran.
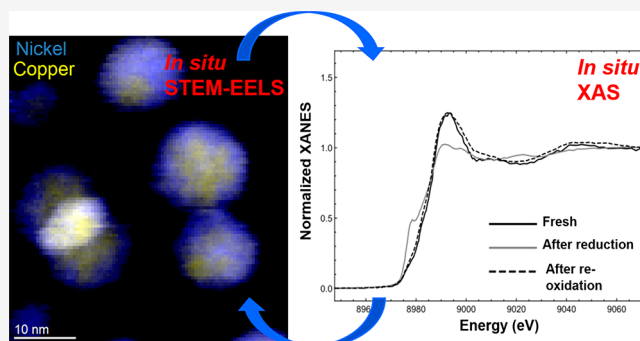
1. INTRODUCTION

Alloyed materials are of great interest for heterogeneous catalysis, as the synergy between metals can lead to improved catalytic properties.[1−3] In particular, Ni−Cu particles are excellent candidates for upgrading lignocellulosic biomass into fuels and other organic components.[4,5] In fact, Ni−Cu systems are used for the hydrodeoxygenation (HDO) of 5-hydroxymethylfurfural (HMF) or the hydrogenation and hydra-rearrangement of furfural (FFA).[6−8] For instance, Ni−Cu nanocatalysts have a high yield for converting HMF to 2,5-dimethylfuran (DMF) because the activity and selectivity of the alloyed Ni−Cu is significantly improved compared to monometallic Ni or Cu.[9,10] A reduction of activity and selectivity is guided by the oxophilicity of the selected elements, as some oxidized metals dramatically weaken the interaction between the catalyst surface and the furan rings. This prevents the overhydrogenation of DMF, thereby increasing the selectivity of the catalyst.[11,8] This emphasizes the impact of the oxidation state on the catalytic properties of Cu−Ni alloys. More generally, the catalytic properties of alloy catalysts (including NiCu) can be modified by changes in the size, shape, metal segregation, and formation of heterogeneities, ultimately impacting the activity and selectivity.[12−14]

The modification of Ni−Cu alloy nanoparticles in a reactive environment is not well understood, as few studies have used in situ diagnostics to track these phenomena. In addition, prior studies provide contradictory explanations about the change of valence states of Cu and Ni in Ni−Cu structures.[15−17] Finally, the kinetics of reduction of this specific alloy has not been investigated in nanoparticles. Exposure to a reactive environment impacts the electronic configuration of the Ni−Cu ensemble, ultimately changing the adsorption and desorption energies.[18−20] Hence, a study of Ni−Cu systems under reductive and oxidative atmospheres is relevant to understand these phenomena. Furthermore, the freshly synthesized particles are often pretreated under H₂ at an elevated temperature (typically 250 °C). Thereafter, the HDO reaction is usually performed at 160−200 °C, which tends to oxidize or reduce the particles, depending on the reaction parameter.[8,6] More generally, Ni−Cu
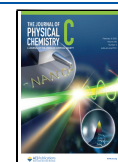
systems are catalysts for a wide range of reactions crucial for industrial processes, where reduction or oxidation of the samples happens at different temperatures. Aside from the HDO of HMF, one can cite the use of Ni−Cu alloys for ethylene hydrogenation[21] where the sample is reduced during pretreatment or the reaction. Hence, long-term exposure to hydrogen and oxygen is an effective and general way to characterize the redox effects during reactions that utilize these materials.

In this work, a correlative, multimodal, in situ analysis was performed on $NiCu_3$ particles supported on amorphous carbon. In situ XAS and in situ STEM-EELS were used to provide information during exposure to realistic conditions. Importantly, this also mitigates the effects of humid air exposure and the reducing environment of high-vacuum characterization when performing ex situ characterization. We reduced and reoxidized freshly synthesized particles to simulate the oxidation and reduction of the system due to the reaction conditions. The goal was to understand the changes in valence state, morphology, and metal distribution that can be expected with $NiCu_3$ particles. With this approach, we saw significant changes in the structure that are likely responsible for the deactivation and reduction in selectivity and activity.

To perform in situ analysis, the sample was sandwiched between two 50 nm SiN windows. The resulting "microreactor" was then inserted into a dedicated holder that allows a flow of gases and controls the temperature using a resistive heating element integrated into one of the two SiN windows.[22] H_2 and O_2 gases were inserted in the microcell through the holder, and the same experimental procedure was performed for in situ XAS and in situ STEM. The temperature was elevated by 50 °C every 30 min under H_2 until 400 °C was reached. The sample was kept at 400 °C under H_2 for 2 h. After 2 h at 400 °C under H_2, the system was cooled to room temperature (RT). Then, the temperature was elevated 50 °C every 30 min under O_2. Once 400 °C was reached, the sample was maintained under these conditions for 1 h. For all experiments, the pressure was 1 bar, and only pure gases were used.

For in situ XAS, collection of data was performed by bringing the specimen back to room temperature under He to suppress noise due to thermal vibrations. In contrast, the sample was kept under elevated temperature and H_2 or O_2 flow for in situ STEM when the data were collected. Indeed, thermal vibrations do not induce significant background signals with STEM-EELS/EDS, so it was unnecessary to cool down the sample under an inert atmosphere for data collection.

This multimodal approach has been developed in previous work to characterize other monometallic or bimetallic samples, such as Pt, Pd, or Pt−Ni nanoparticles.[23−26] It is an advantageous approach to collect data at both the micrometer scale and the millimeter scale that can subsequently be correlated. With in situ XAS, X-ray absorption near-edge structure (XANES) and extended X-ray absorption fine structure (EXAFS) measurements can be performed to determine the change in valence state and coordination numbers.[27−29] With in situ STEM-EELS, valence states can be tracked at the nanoscale level with EELS and elemental mapping with EELS and EDS can determine the distribution of Ni and Cu within individual particles during the cycle.[30,31] For XAS analysis, the experiment was performed at the National Synchrotron Light Source−II beamline for X-ray fluorescent microscopy (XFM) with a $10 \times 10~\mu m^2$ beam size. As demonstrated in our previous experiments with Pt−Ni nanocatalysts,[24] this beam size allows us to obtain maps of the sample

and spectra from different spots to identify regions with distinct valence states at the 10 μm size range.

2. EXPERIMENTAL METHODS

Particle Synthesis and Preparation. Nickel(II) acetylacetonate ($Ni(acac)_2$, 96%) were purchased from Acros Organics., trioctylphosphine (TOP, 97%), copper(II) chloride dihydrate ($CuCl_2·4H_2O$, ≥99%), and oleylamine (OAm, technical grade, 70%) were purchased from Sigma-Aldrich.

NiCu NPs were synthesized based on a previously reported method.[6] $Ni(acac)_2$ (0.1 mmol) and $CuCl_2·2H_2O$ (0.1 mmol) were dissolved in a solution of OAm (20 mL). The reaction mixture was kept at 100 °C for 15 min under vacuum. Then, TOP (3 mmol) was injected into the reaction mixture. The reaction mixture was heated to 230 °C at a rate of 10 °C/min. After 1 h, the reaction mixture was cooled to room temperature. The resulting NPs were purified by precipitation with ethanol and centrifugation at 8000 rpm for 3 min. The precipitate was washed three times with hexane/ethanol (1:3) mixtures, and the final NPs were dispersed in hexane. The unsupported particles in hexane were then mixed with carbon support to achieve a loading of 10 wt % metal. After sonication for 15 min, the solution was centrifuged at 6000 rpm for 1 min. The supernatant was removed, and the precipitate was washed twice with isopropanol, followed by centrifugation. After drying the sample in a vacuum oven overnight at 50 °C, the samples were first treated with an O_2 plasma cleaner (18 W, Harrick Plasma) for 15 min and then transferred for 1 min into a muffle furnace that had been preheated to 500 °C to remove surface organic ligands.

Transmission Electron Microscopy. Scanning transmission electron microscopy (STEM) was performed with an aberration-corrected JEOL NEOARM, operating at 200 kV. A condenser lens aperture of 40 μm was used. For imaging and EDS, a camera length of 4 cm and a probe current of 150 pA were used. For EELS, a camera length of 2 cm and a probe current of 500 pA were used. EELS data were collected with a Gatan K2 camera, a direct-detection camera, to obtain the best signal-to-noise ratio (SNR). A GIF aperture of 5 mm was used, and the energy dispersion was 0.1 eV for all EELS data. For in situ studies (XFM, EELS), an environmental holder for gas-heating experiments manufactured by Hummingbird Scientific was used. The sample was enclosed in a microchip made of two 50 nm Si_3N_4 windows. The lower window contains a heating coil to elevate the temperature inside the cell. The mass flow of gases was controlled with a gas system and software provided by Hummingbird Scientific. The flow rate was 5 sccm. All experiments were carried out under 1 bar.

X-ray Fluorescence Microscopy. XFM was performed at Brookhaven National Laboratory (BNL) at the 4-BM (XFM) beamline of NSLS-II. The Ni K edge (8332.8 eV) and Cu K edge (8978.9 eV) were measured with the sample enclosed in the microchip and the environmental holder provided by Hummingbird Scientific. The gas flow was controlled with a mass flow controller and set to 5 sccm. All in situ data were obtained with a pressure of 1 bar. XFM data were plotted and analyzed with the Athena/Artemis of the Demeter Package. The amplitude reduction factor S_o^2 was 0.836, and all data were collected in fluorescence mode. The beam size was 10 μm and was monochromated by a Si(111) crystal pair. The energy range of the beamline was 4−20 keV.
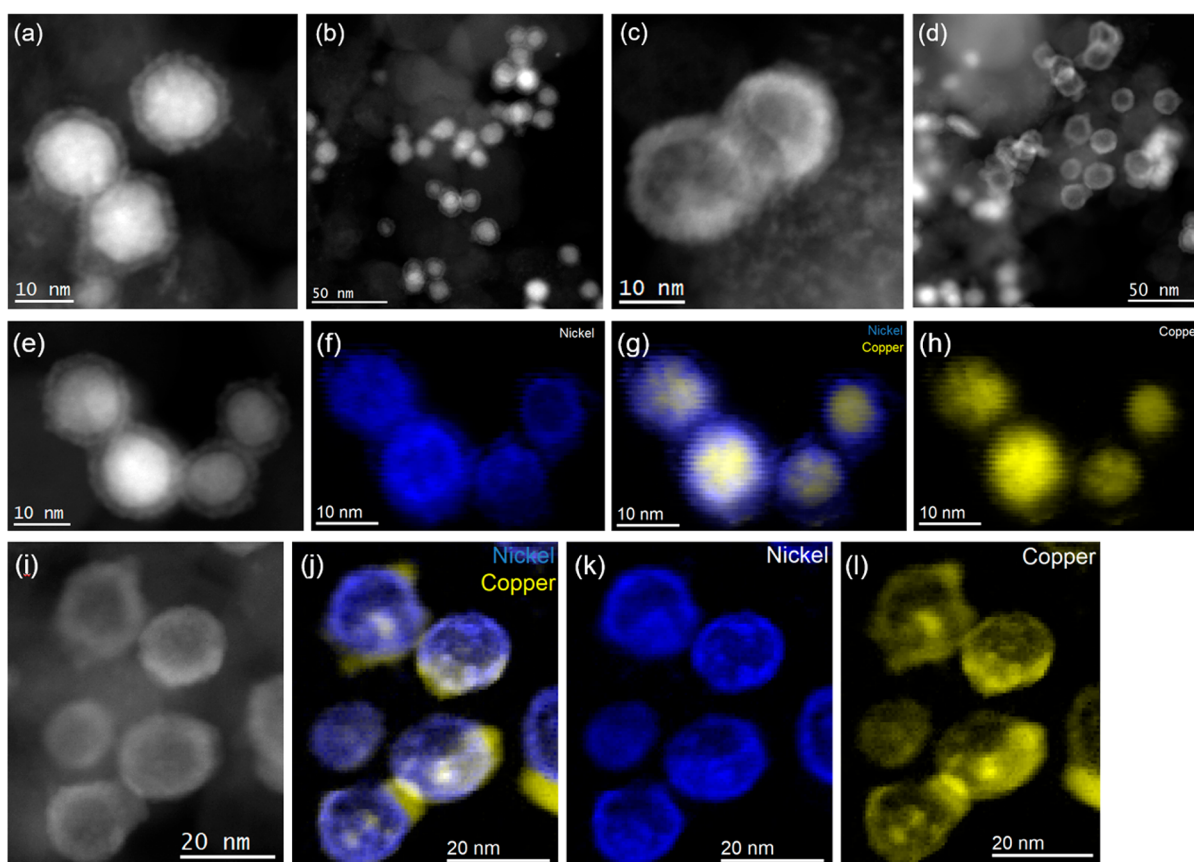
Figure 1. High-angle annular dark-field (HAADF)-STEM imaging and EELS analysis of the sample. (a and b) First morphology observed for most particles. NiO shell envelops the Ni−Cu core. (c and d) Second morphology observed for a minority of particles. Hollow structure is distinguishable with some segregation of Cu. (e) DF-STEM image of particles with the core−shell configuration. (f−h) Combined and separate EELS maps showing a Cu-rich core and Ni-rich shell. (i) DF-STEM image of particles with a hollow structure. (j−l) Combined and separate EELS maps showing a mixed Cu−Ni phase with some segregated Cu. Additional EDS maps are provided in Figures S4 and S5.
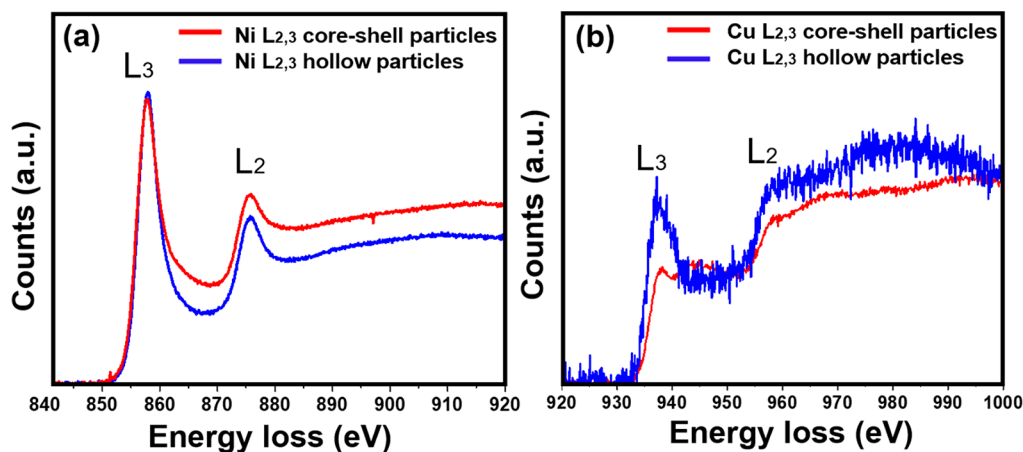
Figure 2. EELS spectra for Ni and Cu. Ni $L_{2,3}$ edges at 855 and 872 eV and Cu $L_{2,3}$ edges at 931 and 951 eV were used. (a) EELS analysis for Ni showing no substantial change between the hollow and the core−shell structures. One can assume that the oxidation state of Ni remains very similar. (b) EELS analysis of Cu showing a substantial difference between the hollow and the core−shell particles. Sharp peak at the L_3 edges indicates that Cu is more oxidized in the former case. A previous publication on the same sample describes the presence of Cu_2O.[32]

3. RESULTS AND DISCUSSION

In all studies shown in this section, $NiCu_3$ particles supported on amorphous carbon were analyzed. Details about the synthesis are provided in the Experimental Methods.

An initial ex situ STEM analysis was performed to understand the structure of the as-synthesized $NiCu_3$ particles deposited on carbon. High-resolution STEM imaging and EELS were performed, and the results are summarized in Figures 1 and 2. The EELS edges used for this analysis were the Ni $L_{2,3}$ edges at 855 and 872 eV and the Cu $L_{2,3}$ edges at 931 and 951 eV.

The high-angle annular dark-field (HAADF)-STEM images in Figure 1 show two morphologies. Both core−shell (Figure 1a and 1b) and hollow structures were observed (Figure 1c and
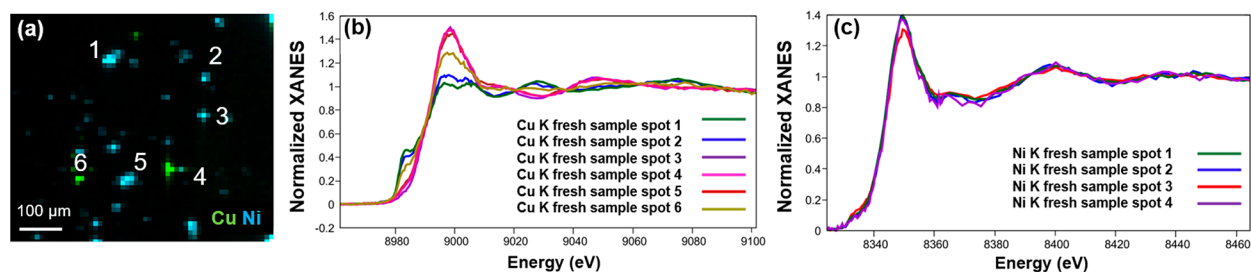
Figure 3. XFM map from the microcell, with XAS signals collected from different spots in the microcell. (a) XFM map showing only the signal for Cu and Ni and underscoring that some areas are very rich in Cu. The sample has compositional heterogeneities at the mesoscale. (b) Cu K edge for 6 clusters of material in the cell. It shows that Cu has different valence states. Some regions are heavily oxidized; others are reduced and nearly metallic. Valence state is not correlated with the signal strength for Cu. (c) Ni K edge for four spots with the metallic Ni foil signal. In this case, Ni remains oxidized with the same valence state, regardless of the location of the sample.
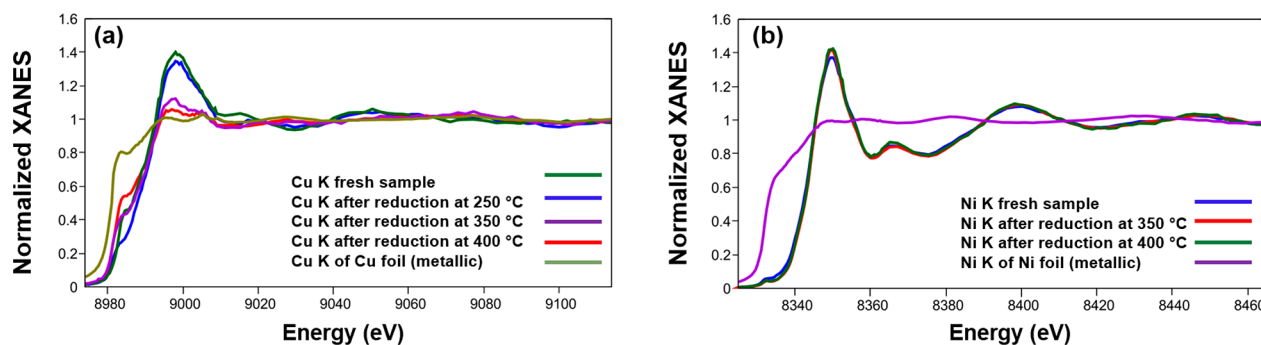
Figure 4. XANES analysis of Cu K and Ni K edges demonstrating changes in the valence states of the two elements. (a) Cu K edge showing progressive but incomplete reduction after prolonged exposure to H_2 at elevated temperature. Temperature was increased by 50 °C every hour until reaching 400 °C under H_2, where the sample was left in these conditions for 2 h. (b) Ni K edges showing no change of the valence state after exposure to H_2 at 400 °C. Mechanism 1 explains the rapid oxidation of metallic Ni with Cu oxide, preventing the formation of Ni metal if the copper remains oxidized. Cu K-edge data of Cu foil (a) exhibits visible self-absorption effects due to the fluorescence measurement mode.

1d). EELS analysis elucidates the composition of the particle: for the core—shell configuration, NiO is present on the surface, and a Ni—Cu mixed phase forms the core (Figure 1e—h). In contrast, O was not very concentrated in the core (Figure S1). The core—shell structure was present in most particles (see Figure S2), an observation consistent with previous studies on the same material.[32] A minority of particles had a hollow configuration with a mixed Cu—Ni phase, although some segregation of Cu was observed (Figure 1i—l). An analysis of over 400 particles showed that 78% were core—shell structures and 22% were hollow structures (Table S1). The existence of the two different configurations is due to the synthesis method as well as exposure to air, as shown in previous publications.[33−37] Also, oxygen was detected everywhere in the hollow particles, including in regions with segregated Cu (Figure S1d). A measurement of 120 particles confirmed that the particles were well dispersed with an average diameter of 12.7 ± 2.6 nm (Figure S3). The particles with the core—shell configuration had approximately the same size as the particles with an empty core.

The hollow particles are formed due to a Kirkendall effect, where oxidation of Cu leads to migration of Cu oxide from the core to the surface. Although the synthesis can be improved to limit this effect, the sample analyzed in this work is representative of Ni—Cu systems, which are not always perfect. Our aim is to study a typical catalyst under realistic conditions instead of focusing on ideal nanoparticles that may not represent the system. In addition, describing the evolution of hollow particles is relevant to understand the evolution of the samples under multiple redox cycles. In fact, prolonged exposure to oxygen may lead to the conversion of core—shell particles into

hollow particles, a result confirmed by further study. Thus, the evolution of the hollow particles is also descriptive of a sample with exclusively core—shell particles that became oxidized during reaction.

In Figure 2, the EELS spectra for the two types of particles indicate a difference in the oxidation state of Cu. Indeed, no dramatic change in the shape of the Ni $L_{2,3}$ edges was observed. However, a sharp peak for Cu L_3 could be clearly distinguished for the hollow configuration and was not observed for the core—shell structure. The sharp peak is called a "white line" and represents energy losses linked to electron transitions from the 2p orbital of Cu to the 3d orbital of Cu(II). Indeed, metallic Cu and Cu(I) have no unoccupied state for the 3d orbital (10 electrons are present), whereas Cu + II has unoccupied states. Hence, the presence of a white line is a signature of Cu(II) oxides. On the basis of the shape of the EELS spectra, it is impossible to determine whether Cu_2O is present or absent in the hollow structure. However, previous XAS studies on the sample indicated the presence of Cu_2O (i.e., Cu(I)). It is thus reasonable to assume that both oxides [Cu(I) and Cu(II)] are present.[32] EELS analysis was also performed for the O K edge at 529 eV, but it was not possible to distinguish a clear difference between the two types of particles (Figure S6).

Thus, hollow particles contain copper oxides, while core—shell particles contain metallic Cu. Hence, we can conclude that morphological differences in the two types of particles observed in the sample are linked to different oxidation levels of Cu.

After completing the initial ex situ STEM study, the sample was analyzed with in situ characterization techniques. First, the NiCu$_3$ catalyst was examined at a beamline for X-ray
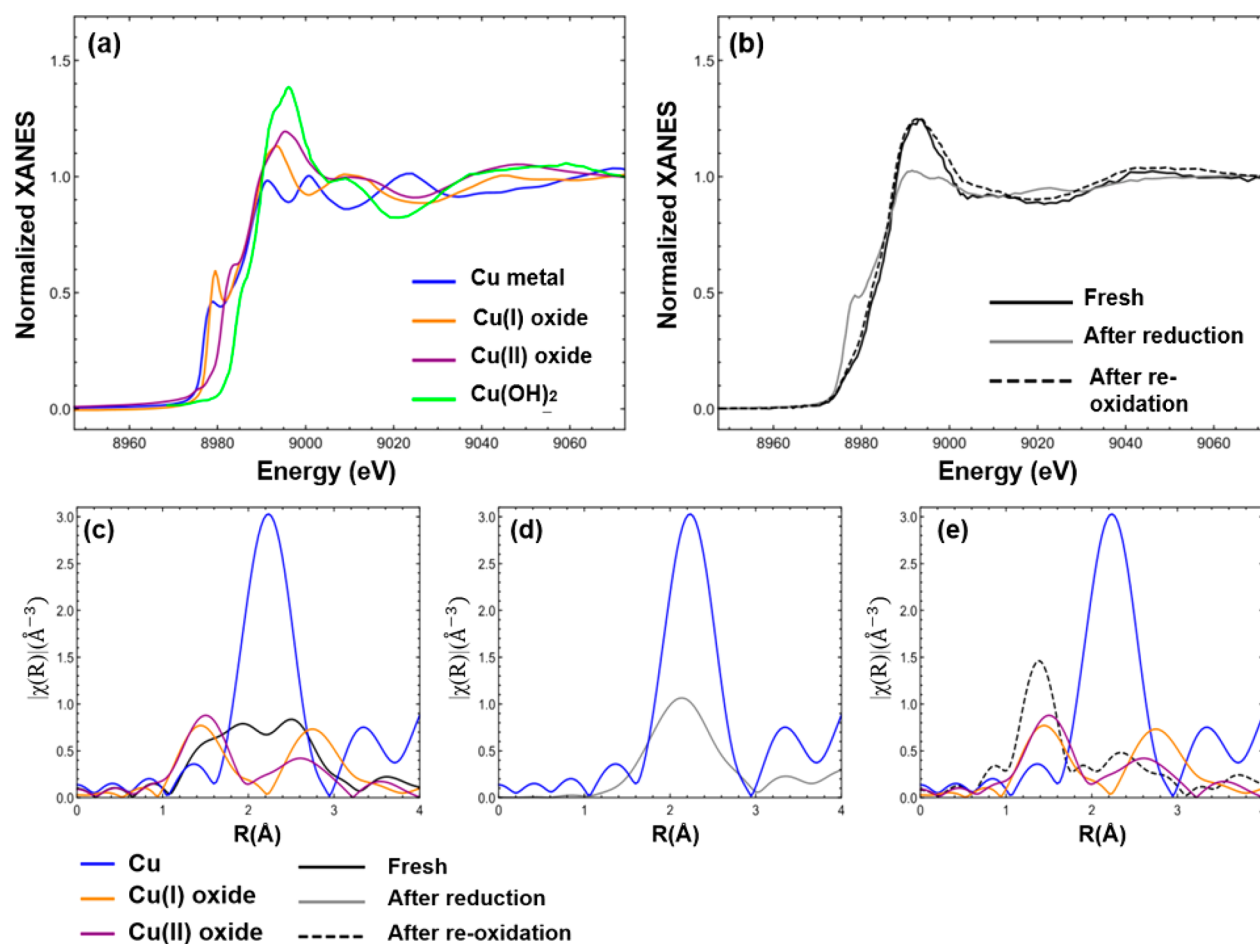
Figure 5. XANES and Fourier transform (FT)-EXAFS data of the sample, containing the two configurations, during the redox cycle. Cu K edge was used. (a) Reference XANES spectra for Cu species. (b) XANES of the experimental data: fresh, after reduction, and after reoxidation. (c) FT-EXAFS of fresh sample with reference spectra of Cu species. (d) FT-EXAFS of reduced sample with reference spectra of Cu species. (e) FT-EXAFS of reoxidized sample with reference spectra of Cu species.

Table 1. EXAFS Analysis of the NiCu$_3$ Sample during the Redox Cycle^a

state	$N_{(Cu-M)}$	$N_{(Cu-O)}$	$R_{(Cu-M)}$	$R_{(Cu-O)}$	$\sigma^2_{(Cu-M)}$	$\sigma^2_{(Cu-O)}$
fresh	5 (2)	2.4 (8)	2.61 (2)	2.07 (4)	0.010 (5)^b	0.010 (5)^b
reduced	5 (1)		2.51 (1)		0.010 (2)	
oxidized	0.7 (3)	2.6 (5)	2.47 (2)	1.87 (2)	0.001 (2)^b	0.001 (2)^b

^{a}The sample was cooled to room temperature under helium to collect EXAFS data. Cu−M and Cu−O bonds were fitted with a theoretical model for NiCu$_3$. N is the coordination number, R is the interatomic distance, and Debye−Waller factors are indicated by σ^2. The uncertainties in the last significant digits are shown in parentheses. A continuous drop of Cu−M coordination number (CN) suggests a change of morphology. For the re-oxidized sample, a stronger signal was observed for the Cu−O bonds, indicating that Cu becomes more oxidized than in the as-synthesized form. ^{b}Variable was constrained for both the Cu−M and the Cu−O paths.

fluorescence microscopy (XFM). To this end, the sample was enclosed in a microcell made of two Si$_3$N$_4$ windows and exposed to gases and elevated temperature while being irradiated with an X-ray microbeam. The cell also contained a microcoil in one Si$_3$N$_4$ window and was mounted on a dedicated holder for gas experiments. The beam had a diameter of 10 μm and could spatially resolve aggregates of NiCu$_3$/C sample in the cell. A schematic of the microcell is shown in Figure S7.

Figure 3 provides XAS data from the fresh sample inside the microcell, before in situ analysis was started. The investigation of the origin of the Ni-rich regions will be the topic of a future work. The Ni K edge (8332.8 eV) and Cu K edge (8978.9 eV) were used in the in situ XAS study. In Figure 4a, an XAS map of the microcell was collected and groups of NiCu$_3$ particles can be

seen. These regions are aggregations of amorphous carbon supporting many NiCu$_3$ particles. The data show that some clusters are richer in Cu (green) and others are richer in Ni (blue). Hence, it is possible to conclude that the sample has compositional heterogeneity at a 10 μm level. The origin of compositional heterogeneities at the micrometer scale is not clear to us, especially since the Ni/Cu ratio was the same for hollow and core−shell particles.

Interestingly, some regions have metallic Cu while others have oxidized Cu. The oxidation of Cu was not correlated with areas where the Cu signal was stronger. We assume that the regions with a higher oxidation state for Cu contain more hollow particles, considering the STEM/EELS results shown in Figure 2. In contrast, regions with metallic Cu are more likely to display
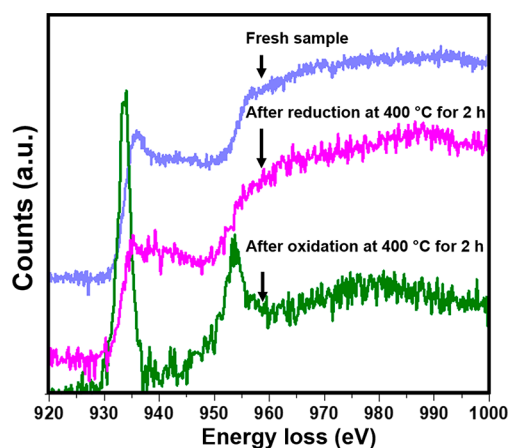
Figure 6. EELS spectra for the Cu $L_{2,3}$ edges at 931 and 951 eV loss. For each spectrum, a representative group of 5−10 particles was used. Shifts in the valence state of Cu can be observed with the disappearance and reappearance of white lines at 931 and 951 eV. Cu was reduced upon exposure to H_2 at 400 °C for 2 h and became heavily oxidized upon reoxidation. These results are consistent with XANES data in Figure 5.

mostly core−shell structures, as described in the ex situ STEM analysis. This seems the most likely explanation for the spatial differences of Cu oxidation state, especially since we observed regions very rich in either core−shell or hollow particles (see Figure S8). Ni remains oxidized regardless of the spatial position of the sample. This observation is consistent with our initial ex situ STEM-EELS data in Figure 2. Previous work showed that NiO is the dominant oxide in fresh NiCu$_3$ and upon reduction.[32] In addition, a comparison of the Fourier transform magnitude of the Ni signal with reference plots for metallic Ni and NiO suggests that NiO is present in the sample (see Figure S9).

After XAS analysis of the fresh sample, the sample was exposed to H_2 at 400 °C for 2 h, following the procedure described in the Introduction. Data were collected 30 min after the temperature reached 250 and 350 °C. Then, the sample was exposed to O_2 at 400 °C for 1 h.

Figure 4 shows the XANES edge for Cu K and Ni K under H_2 as the temperature was increased by 50 °C every hour. Cu is reduced (Figure 4a), while Ni remains oxidized (Figure 4b) with the same valence state. The reduction of Cu appears to accelerate at temperatures above 250 °C. The Fourier magnitude of the EXAFS data for the reduced sample (see Figure 5) is also consistent with a reduction of Cu. The prominent peak at 2.1 Å of the reduced sample is close to the reference signal for metallic Cu. Although a clear reduction of Cu is observed, it is not possible to rule out the presence of small amounts of Cu oxides. This point will be addressed in the STEM-EELS analysis, described below.

The selective reduction of Cu is not surprising: In fact, the nobility of Cu is higher than that of Ni.[38] However, one might have thought that some Ni would be reduced too, as we observed hollow structures with Ni on the surface (Figure 1j). A mechanism leading to the formation of metallic copper in Ni−Cu alloys has been proposed in previous publications, and we believe it applies to the particles studied in this work.[15] A diffusion-controlled displacement reaction happens according to the following equation

$$Ni + Cu_2O \rightarrow NiO + 2Cu \tag{1}$$
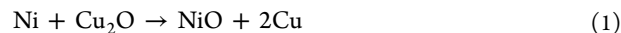
At elevated temperature, reduction of Ni immediately leads to a reaction with copper oxide to form nickel oxide and metallic copper. Previous analyses have suggested that this reaction can occur, leading to some segregation of nickel-rich and copper-rich phases.[15] This is consistent with what we see here: it is
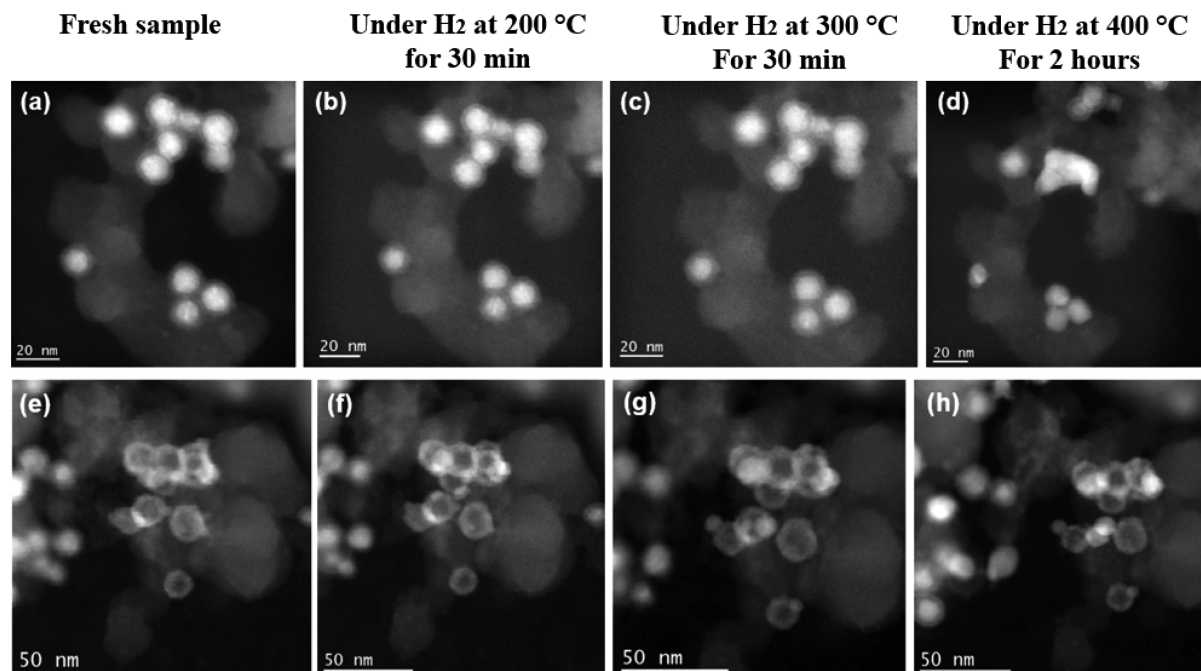
Figure 7. HAADF-STEM images showing the effect of reduction on the morphology of the two types of particles. (a−d) Core−shell particles. Core−shell configuration is not visible on the images after prolonged exposure to H_2 at 400 °C. Many particles appear to become mixed Cu−Ni phases, although it is possible that a thin layer of NiO on the surface might still be present. Some core−shell particles are still clearly visible in d. (e−h) Hollow particles. Progressive and slow disintegration of the hollow structure was visible, although incomplete. Formation of solid spheres on the surface of the hollow particles was also visible.
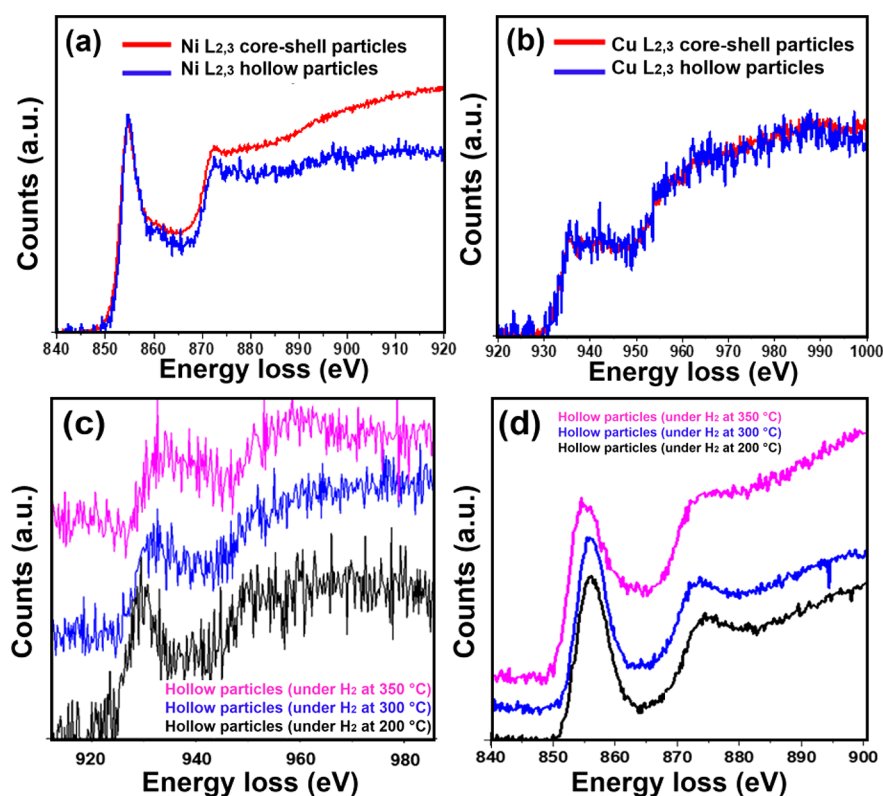
Figure 8. EELS edges for the reduced NiCu$_3$ sample. (a) Ni L$_{2,3}$ edges for the core–shell and hollow particles after reduction under H$_2$ at 400 °C. Shape of the edges is similar to the edges collected for the fresh sample in Figure 2a. This is also consistent with Figure 3c. (b) Cu L$_{2,3}$ edges for the core–shell and hollow particles after reduction under H$_2$ at 400 °C. Edges show the complete reduction of Cu and prove that core–shell and hollow particles converge to the same valence state. (c) Tracked Cu L$_{2,3}$ edges of the same clusters of hollow particles being progressively reduced after exposure to H$_2$. Progressive reduction of the hollow particles correlates the average reduction of Cu observed in the XANES data. (d) Tracked Ni L$_{2,3}$ edges of the same clusters of hollow particles analyzed in c being progressively reduced after exposure to H$_2$. No changes in the edge can be detected, underlining that Ni does not seem to be changed during the reduction process.

consistent with the XANES data and the difficulty of reducing Ni when metallic copper is produced. Once all of the copper has been reduced, one can postulate that Ni will form a metallic phase. This was observed in a controlled reaction where Ni became metallic after a 2 h treatment under H$_2$ above 550 °C to accelerate the process (Figure S10). Reaction 1 has been postulated for large volumes of Ni–Cu alloy, and the XAS experiments indicate that this reaction is still valid for nanostructures.

After reduction under H$_2$ at 400 °C, the sample was exposed to O$_2$ at 400 °C. Figure 5 provides XANES-EXAFS data of reference Cu-based samples and the fresh, reduced, and reoxidized NiCu$_3$ sample. All XANES-EXAFS data in Figure 5 were obtained by merging multiple XANES-EXAFS spectra from different locations in the cell in order to enhance the signal-to-noise. Figure 5a provides reference spectra for metallic Cu, Cu(I) oxide, Cu(II) oxide, and Cu(OH)$_2$. Figure 5b provides XANES data of the whole sample at the beginning of the experiment, after reduction, and after oxidation. At the beginning (black curve in Figure 5b), Cu appears partially oxidized. A subtle absorption peak at 8978 eV can be visible. The presence of the absorption peak is a signature for reduced Cu. In contrast, the absence of an absorption peak indicates an oxidized state for Cu. After reduction (gray curve), this peak is more prominent. After reoxidation (dotted curve), no absorption peak is visible. Hence, one can conclude that the sample becomes more oxidized upon reoxidation compared to the initial state.

After reoxidation, the disappearance of the absorption peak at 8978 eV shows that Cu is as nearly completely reoxidized.

The EXAFS signals from the same spectra were then analyzed. The results are summarized in Table 1, where the Cu–M (Metal) and Cu–O bonds of NiCu$_3$ were used to fit the EXAFS results. The local parameters, e.g., coordination numbers (CN) and the bond lengths (R), are provided in Table 1 for both the Cu–M and the Cu–O contributions. The magnitude of the Fourier transform of the k^2-weighted EXAFS data and k^2-weighted fits are provided in Figure S11. Local parameters for bulk Cu references are provide in Table S2.

For the fresh sample, EXAFS was fit with the Cu–O and Cu–M contributions (M can be either Ni or Cu: they cannot be distinguished), indicating a combination of alloy and oxide phases. The oxide phase is in the Cu(II) oxidation state based on the XANES data (Figure 5a and 5b). The Cu–M bond is much shorter than expected for an oxide, and thus, it may be due to the combination of Cu bonding in oxide and alloy phases. In addition, the Cu–M CN is low (5 ± 2 vs 12, which is expected in the bulk fcc structure). There are various sources of under-coordinated Cu in the sample, as evident by STEM. These include small Cu regions with a high surface area to volume ratio of Cu, the inside surfaces of the hollow spheres, and between the alloy and oxide interfaces. Since the fresh sample is a combination of alloy and oxide phases, we cannot comment on the specific source solely from EXAFS analysis.

For the reduced sample, EXAFS was successfully fit with only Cu–M contributions, which is not surprising given that XANES
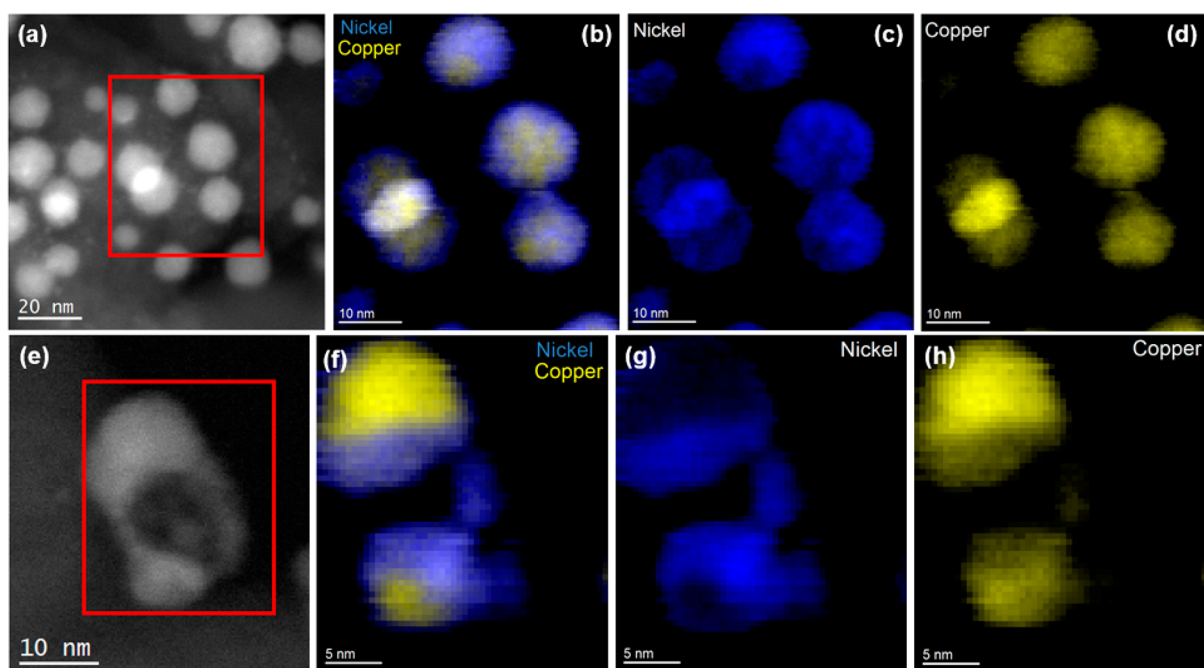
Figure 9. EELS maps of the two types of particles after reduction under H$_2$ at 400 °C for 2 h. Red boxes in a and e indicate the regions mapped with EELS. (a) Initial core−shell structure after reduction with no visible shell on the HAADF-STEM image. (b−d) EELS maps show the presence of a thin Ni-rich surface. Thus, reduction did not completely destroy the core−shell configuration. (e) Initial hollow particle after reduction. Protuberance was formed during reduction at elevated temperatures. (f−h) EELS maps indicate the segregation of Cu in the protrusion. Cu appears more exposed to the environment, which could explain the complete reduction.
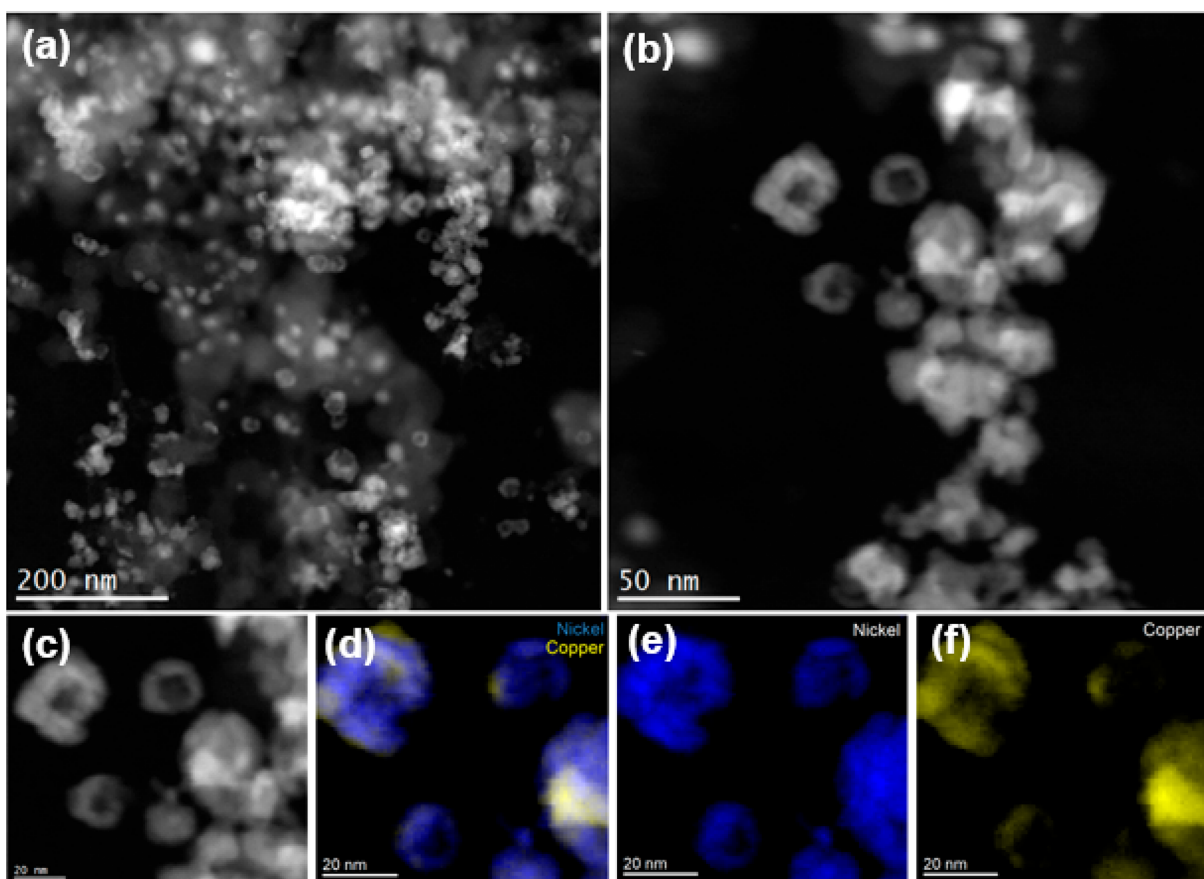
Figure 10. HAADF-STEM image of the sample after reoxidation at 400 °C under O$_2$. Change of morphology is rapid and happens within 30 min. (a−c) Low- and high-magnification HAADF-STEM images showing the dominance of the hollow particle configuration. (d−f) EELS maps for Ni and Cu showing compositional heterogeneities, as Cu and Ni do not remain fully mixed.

indicates metallic Cu(0) (Figure 5a and 5b). Surprisingly, the Cu−M coordination number remains very low, 5 ± 1. One would expect the reduction of Cu to increase the CN of the Cu−M bonds at elevated temperatures under H_2. In this case, we can be sure that the source of undercoordination is coming from metallic Cu or alloy Cu−Ni regions due to the lack of Cu−O bonding. Small Cu regions, seen in Figure 1, and the high surface area to volume ratio of the hollow particles are the likely source of such a small coordination number. In addition, a decrease in the Cu−M distances (from 2.61 to 2.51 Å) is observed upon reduction. This could be due to the removal of oxygen atoms in the Cu−Ni random alloy.

For the reoxidized sample, EXAFS was fit with only Cu−M and Cu−O contributions from the Cu oxide phase. While the XANES (Figure 5a and 5b) and EXAFS (Figure 5e) results of the sample resemble Cu(II) oxide, the fitted coordination numbers of Cu−M (0.7 ± 0.3) and Cu−O are smaller than expected (2.6 ± 0.5). While we cannot rule out the presence of metallic Cu−M or alloy Cu−M contributions, we can say that the reoxidized sample in EXAFS (and XANES) is dominated by Cu(II) oxide after the reoxidation process of the reduction−oxidation cycle. This is consistent with subsequent in situ STEM analysis, described below.

It is not possible to determine the morphology of the particles during the redox cycle with the present EXAFS data. In addition, the XANES-EXAFS data samples many nanoparticles, and it is impossible to determine dynamical changes at the nanoscale level on individual particles by an average method if a broad distribution of particle sizes, different morphologies, and compositional distributions are present. Finally, the total reduction of Cu is unclear as it was not possible to rule out the presence of Cu oxides solely based on XANES-EXAFS analysis.

Hence, an in situ STEM-EELS analysis was conducted to complement and refine the information obtained from XANES-EXAFS. To this end, the same experimental procedure was performed, a fresh sample was enclosed in the same micro-reactor, and identical reaction conditions were utilized. EELS data for the Cu $L_{2,3}$ edges at 931 and 951 eV during the redox cycle are summarized in Figure 6. The spectra were collected on 5−10 particles with representative configurations. For the fresh sample, a small white line was visible for the Cu L_3 edge, indicating some oxidation of Cu. Theoretically, a white line is also present for the Cu L_2 edge, but it is harder to distinguish because the L_2 edge is smaller than the L_3 edge. After reduction, no white line was present, indicating the reduction of Cu. The absence of white lines indicates a complete reduction of Cu. Hence, we concluded that Cu oxides were no longer present in the sample. Upon reoxidation, the white lines are much more prominent than at the beginning, indicating that more Cu is oxidized after reoxidation than at the beginning. These results are consistent with the XANES data in Figure 5. Hence, we can conclude that shifts in the valence state of Cu are the same for a large set of particles (thousands for XANES data) and a small group of particles (5−10 particles analyzed with STEM-EELS).

The data shown in Figure 6 were collected from a group of nanoparticles upon reduction and reoxidation without considering the impact of morphology. However, the preliminary ex situ STEM-EELS study underlined a correlation between the valence state of Cu and the morphology: Cu is more oxidized in the hollow particles than in the core−shell structure. To explore this further, STEM images were collected during the reduction and reoxidation of the sample. In Figure 7, we show the

structural changes for core−shell and hollow particles during reduction. It is possible to notice the disappearance of the visible core−shell structure, especially after prolonged exposure to H_2 at 400 °C. Figure 7 also shows a reduction in the particles' diameter upon reduction and destruction of the core−shell morphology. This agrees with our hypothesis based on the EXAFS analysis of the data after reduction. Indeed, the EXAFS data showed no increase of the Cu−M CN after reduction. Hence, we hypothesized a reduction of the diameter of the particles is offsetting the increase in Cu−M CN due to the reduction of Cu. Some core−shell particles remain unchanged at the end of the reduction, as they keep a thick NiO shell (Figure S12). A spherical structure with a solid core is also formed for the hollow particles during the cycle, although the rate appears to be slower. Some hollow particles remain after reduction.

Subsequently, an EELS analysis on the two types of particles was performed after reduction. The EELS spectra for the Ni $L_{2,3}$ and Cu $L_{2,3}$ edges are shown in Figure 8 and again confirm the reduction of Cu in both configurations. The results are complementary with the XANES-EXAFS analysis, where it was impossible to distinguish between core−shell and hollow particles. Figure 8a shows no difference in the valence state of Ni. Figure 8b indicates the absence of Cu oxides, as no white line can be seen for the hollow and the core−shell particles. Thus, we can conclude that Cu was fully reduced in both types of particles. The collected EELS signal for Ni is very similar to that of the fresh sample, indicating that Ni keeps the same valence state, again consistent with the XANES-EXAFS results. In Figure 8c and 8d, we specifically tracked the same cluster of hollow particles during reduction. The changes in the shape of the Cu $L_{2,3}$ edges suggest a progressive reduction, while no changes could be seen with the Ni $L_{2,3}$ edges. This is consistent with mechanism 1, which we suggested to explain the reduction of Cu without altering Ni in hollow particles.

EELS maps were obtained to understand the NiO and Cu distribution in the particles after reduction (Figure 9) for the two types of particles. For the particles that initially had the core−shell morphology (majority of particles), a thin shell of Ni remains even after reduction (Figure 9a−d). Hence, the HAADF-STEM images in Figure 7 correspond to a thinning of the NiO shell enveloping the core, but it did not completely disappear. Also, based on XANES, we know that Ni was not reduced, so we can conclude that a NiO shell is still present on the surface. Thus, the EELS maps appear to be a useful complement to STEM imaging, as the NiO layer could not be seen based solely on HAADF image contrast.

For the particles with an initial hollow structure, formation of a protrusion with bulk Cu was observed (Figure 9e−h). The segregation of Cu on the outside of the hollow structure may be correlated with the reduction of the metal. Indeed, Cu atoms are no longer embedded in a Cu−Ni phase, but a large volume of Cu becomes clearly exposed to the surface and is quickly reduced by the H_2-rich environment. This explains the EELS data for the Cu edge in Figure 8b.

After reoxidation, the shape of the particles changed dramatically. The transformation is rapid and happens within 30 min after 400 °C under O_2 was reached. Nearly all particles had a hollow structure, as shown in the HAADF-STEM images in Figure 10, with segregation of Cu and Ni observed. The morphology, combined with Cu segregation, could explain the low coordination number for the Cu−M bonds calculated with EXAFS. Indeed, the transformation from solid spheres to hollow particles reduces the total number of Cu−M bonds. Most of the

Cu atoms are exposed to the surface and can be easily oxidized. The configuration also explains the sharp increase in the oxidation state of Cu with the prominent white lines observed in Figure 7.

Figure 10 shows trends observed for the majority of particles, but some exceptions were observed. The in situ STEM images in Figure S13 show that very small particles have formed in some regions on the carbon support. These structures are formed during the reduction of the sample at elevated temperatures but do not disappear after oxidation. Hence, STEM imaging indicates an irreversible change in the specimen. EDS and EELS analyses show that the tiny particles are made of NiO (see Figure S14), so one can conclude that some particles have an increased Cu:Ni ratio upon cycling. The migration of Ni on the surface of the amorphous carbon film also causes a reduction of the size of the particles. This can also explain the EXAFS data showing an unchanged coordination number of Cu−M bonds upon reduction.

The substantial differences in the shape and composition can be linked to the catalytic properties of the materials for the HDO to HMF, as an example. It has been shown that this $NiCu_3/C$ system is highly active for the HDO of HMF into DMF.[8] It has also been shown that the activity of the Ni−Cu nanoparticles slightly decreases after 4 h of reaction, without evidence of sintering and with oxidation of the sample during reaction.[32,8] This leads us to believe that the changes in the particles' configuration observed during the redox experiment might be the cause of the lower DMF yield. In fact, it is known that the Ni−Cu systems exhibit enhanced catalytic properties for the HDO of HMF compared to their monometallic parents. A hypothesis for this improvement is the hindrance of furan rings to lie down on catalysts that have an alloyed structure. This prevents overhydrogenation of DMF into unwanted products.[39,40] Another explanation is the stronger adsorption of the C=O group on the alloyed surface compared to pure metals, leading to a better activity.[41] Another assumption is the role of the surface oxide that catalyzes HMF through the scission of C−O bonds following a reverse Mars−Van Krevelen mechanism.[42,43]

Since $NiCu_3/C$ particles exhibit high catalytic properties at the beginning of the HDO of HMF, we can assume that the core−shell configuration present in most particles is beneficial as the presence of surface oxide leads to a reverse Mars−Van Krevelen mechanism. Even though particles are pretreated before reactions, we have shown that a very thin layer of NiO remains on the surface of the particles. Most pretreatments were performed under H_2 at temperatures below 400 °C. However, the presence of initial hollow particles with a strong degree of segregation between the two metals and the absence of a core−shell configuration may reduce the activity. The presence of Cu metal on the surface of hollow particles under reduction, as seen in Figure 9f, may cause the furan rings to lie down on the metallic Cu, leading to overhydrogenation. In addition, Cu and Ni appear to be strongly segregated in the hollow particles after reduction at 400 °C, which will impact the synergetic effects of both metals.

Oxidation of the samples shows a loss of core−shell configurations with a high degree of segregation between Cu and Ni. This can cause the noticeable drop in activity observed in a previous publication.[8] Since strong segregation of Cu and Ni was observed in the reoxidized sample, we can speculate that the synergy between Ni and Cu is lost for the HDO and HMF and that the sample acts as a monometallic system.

Finally, it should be noticed that overoxidation of the sample does not seem reversible. Hence, the deactivation of the catalyst observed after prolonged exposure to reaction conditions might not be offset with exposure to H_2 at elevated temperatures. Indeed, most particles had a hollow structure after reoxidation, as seen in Figure 10. When reduced, the data show that the hollow structures have a high degree of segregation, as shown in Figure 9e−h and the EXAFS analysis (Table 1). Hence, the system will likely have an activity for the HDO of HMF equivalent to monometallic Cu or Ni. Cu is more exposed to the surface after reoxidation, so we expect this will change the yield of DMF: it has been shown that greater interaction between the furan rings and nonoxidated surfaces yields overhydrogenation of DMF.[44]

4. CONCLUSION

In conclusion, this study demonstrates the complex dynamics behind valence state changes and the composition of Ni−Cu systems. The in situ XAS studies proved that the Ni valence state is unchanged while Cu is reduced upon exposure to H_2 at 400 °C. It is in part due to a diffusion-controlled displacement reaction where metallic Ni quickly reacts with copper oxide to form metallic copper and nickel oxide. The reduction of Cu is rapid, especially at temperatures above 250 °C. EXAFS analysis underlines the reduction of Cu, and the low CN for Cu−M is due to segregation between Cu and Ni in the fresh, reduced, and reoxidized sample. In addition, hollow particles with a thin shell contribute to the low CN for the Cu−M bonds. The in situ STEM-EELS/EDS results confirm and refine the results collected with in situ XAS. The shape of the initial core−shell and hollow particles evolves differently. In both cases, full reduction of Cu is achieved. Upon reoxidation, nearly all particles display a hollow structure with a highly oxidized Cu phase. During the whole redox cycle, full mixing of Cu and Ni was never achieved and reduction of NiO was not possible. In the specific example of the HDO of HMF, the presence of a NiO shell enveloping a NiCu core seems to be beneficial to keep an oxidized surface, preventing overhydrogenation of DMF. However, strong segregation of Cu and Ni upon oxidation will impact the catalytic activity of the sample as synergy between Cu and Ni is lost.

This study underlines the complexity of alloyed catalysts, which cannot necessarily be described with a single morphology or chemical configuration. Understanding subtle heterogeneities of nanostructures is a necessary step to improve functional nanomaterials. This combined in situ studies with STEM-EELS/EDS and XFM can be applied to a wide range of samples used for industrial processes and can guide the design of novel materials with enhanced performance and stability.[45−49]

■ ASSOCIATED CONTENT

ⓈI Supporting Information

The Supporting Information is available free of charge at https://pubs.acs.org/doi/10.1021/acs.jpcc.1c10824.

> Particle size distribution; additional STEM images; EELS and EDS data; additional XANES and EXAFS data; details about EXAFS analysis (PDF)

■ AUTHOR INFORMATION

Corresponding Author

Eric A. Stach − *Department of Materials Science and Engineering, University of Pennsylvania, Philadelphia,*

Pennsylvania 19104, United States; Laboratory for Research on the Structure of Matter, University of Pennsylvania, Philadelphia, Pennsylvania 19104, United States; orcid.org/0000-0002-3366-2153; Email: stach@seas.upenn.edu

Authors

Alexandre C. Foucher − Department of Materials Science and Engineering, University of Pennsylvania, Philadelphia, Pennsylvania 19104, United States; orcid.org/0000-0001-5042-4002

Nicholas Marcella − Department of Materials Science and Chemical Engineering, Stony Brook University, Stony Brook, New York 11794, United States; orcid.org/0000-0002-2224-532X

Jennifer D. Lee − Department of Chemistry and Chemical Biology, Harvard University, Cambridge, Massachusetts 02138, United States; Department of Chemistry, University of Pennsylvania, Philadelphia, Pennsylvania 19104, United States

Ryan Tappero − Photon Sciences Department, Brookhaven National Laboratory, Upton, New York 11973, United States

Christopher B. Murray − Department of Materials Science and Engineering, University of Pennsylvania, Philadelphia, Pennsylvania 19104, United States; Department of Chemistry, University of Pennsylvania, Philadelphia, Pennsylvania 19104, United States

Anatoly I. Frenkel − Department of Materials Science and Chemical Engineering, Stony Brook University, Stony Brook, New York 11794, United States; Division of Chemistry, Brookhaven National Laboratory, Upton, New York 11973, United States; orcid.org/0000-0002-5451-1207

Complete contact information is available at:
https://pubs.acs.org/10.1021/acs.jpcc.1c10824

Notes

The authors declare the following competing financial interest(s): One of the authors (E.A.S.) has an equity interest in Hummingbird Scientific.

ACKNOWLEDGMENTS

REFERENCES

(1) Wu, C. H.; Liu, C.; Su, D.; Xin, H. L.; Fang, H.-T.; Eren, B.; Zhang, S.; Murray, C. B.; Salmeron, M. B. Bimetallic Synergy in Cobalt−Palladium Nanocatalysts for CO Oxidation. Nat. Catal. 2019, 2 (1), 78−85.

(2) Singh, A. K.; Xu, Q. Synergistic Catalysis over Bimetallic Alloy Nanoparticles. ChemCatChem. 2013, 5, 652−676.

(3) Zafeiratos, S.; Piccinin, S.; Teschner, D. Alloys in Catalysis: Phase Separation and Surface Segregation Phenomena in Response to the Reactive Environment. Catal. Sci. Technol. 2012, 2, 1787−1801.

(4) Wang, P.; Jing, Y.; Guo, Y.; Cui, Y.; Dai, S.; Liu, X.; Wang, Y. Highly Efficient Alloyed NiCu/Nb$_2$O$_5$ catalyst for the Hydro-deoxygenation of Biofuel Precursors into Liquid Alkanes. Catal. Sci. Technol. 2020, 10, 4256−4263.

(5) Den, W.; Sharma, V. K.; Lee, M.; Nadadur, G.; Varma, R. S. Lignocellulosic Biomass Transformations via Greener Oxidative Pretreatment Processes: Access to Energy and Value Added Chemicals. Frontiers in Chemistry. 2018, 6, 141.

(6) Lee, J. D.; Wang, C.; Jin, T.; Gorte, R. J.; Murray, C. B. Engineering the Composition of Bimetallic Nanocrystals to Improve Hydro-deoxygenation Selectivity for 2-Acetylfuran. Appl. Catal. A Gen. 2020, 606, 117808.

(7) Luo, J.; Yun, H.; Mironenko, A. V.; Goulas, K.; Lee, J. D.; Monai, M.; Wang, C.; Vorotnikov, V.; Murray, C. B.; Vlachos, D. G.; et al. Mechanisms for High Selectivity in the Hydrodeoxygenation of 5-Hydroxymethylfurfural over PtCo Nanocrystals. ACS Catal. 2016, 6, 4095−4104.

(8) Luo, J.; Monai, M.; Wang, C.; Lee, J. D.; Duchoň, T.; Dvořák, F.; Matolín, V.; Murray, C. B.; Fornasiero, P.; Gorte, R. J. Unraveling the Surface State and Composition of Highly Selective Nanocrystalline Ni-Cu Alloy Catalysts for Hydrodeoxygenation of HMF. Catal. Sci. Technol. 2017, 7, 1735−1743.

(9) Sun, Y.; Xiong, C.; Liu, Q.; Zhang, J.; Tang, X.; Zeng, X.; Liu, S.; Lin, L. Catalytic Transfer Hydrogenolysis/Hydrogenation of Biomass-Derived 5-Formyloxymethylfurfural to 2, 5-Dimethylfuran over Ni-Cu Bimetallic Catalyst with Formic Acid As a Hydrogen Donor. Ind. Eng. Chem. Res. 2019, 58, 5414−5422.

(10) Seemala, B.; Cai, C. M.; Wyman, C. E.; Christopher, P. Support Induced Control of Surface Composition in Cu-Ni/TiO$_2$ Catalysts Enables High Yield Co-Conversion of HMF and Furfural to Methylated Furans. ACS Catal. 2017, 7, 4070−4082.

(11) Kepp, K. P. A Quantitative Scale of Oxophilicity and Thiophilicity. Inorg. Chem. 2016, 55, 9461−9470.

(12) Luneau, M.; Guan, E.; Chen, W.; Foucher, A. C.; Marcella, N.; Shirman, T.; Verbart, D. M. A.; Aizenberg, J.; Aizenberg, M.; Stach, E. A.; Madix, R. J.; Frenkel, A. I.; Friend, C. M.; et al. Enhancing Catalytic Performance of Dilute Metal Alloy Nanomaterials. Commun. Chem. 2020, 3, 46.

(13) Luneau, M.; Shirman, T.; Foucher, A. C.; Duanmu, K.; Verbart, D. M. A.; Sautet, P.; Stach, E. A.; Aizenberg, J.; Madix, R. J.; Friend, C. M. Achieving High Selectivity for Alkyne Hydrogenation at High Conversions with Compositionally Optimized PdAu Nanoparticle Catalysts in Raspberry Colloid-Templated SiO$_2$. ACS Catal. 2020, 10, 441−450.

(14) Lee, J. D.; Jishkariani, D.; Zhao, Y.; Najmr, S.; Rosen, D.; Kikkawa, J. M.; Stach, E. A.; Murray, C. B. Tuning the Electrocatalytic Oxygen Reduction Reaction Activity of Pt-Co Nanocrystals by Cobalt Concentration with Atomic-Scale Understanding. ACS Appl. Mater. Interfaces 2019, 11, 26789−26797.

(15) Evans, T. E.; Fleetwood, M. J. Oxidation of Cupro-Nickel Alloys in Steam-Oxygen Mixtures. Nature 1962, 196, 164−165.

(16) Levin, R. L. The Role of a Displacement Reaction in the Kinetics of Oxidation of Alloys. Ph.D. Dissertation, Yale University, New Haven, CT, 1961.

(17) Castle, J. E.; Harrison, J. T.; Masterson, H. G. Oxidation of Cupro-Nickel Alloys in Steam-Oxygen Mixtures. Nature 1962, 196, 261−262.

(18) Das, S. K.; Das, A.; Gaboardi, M.; Pollastri, S.; Dhamale, G. D.; Balasubramanian, C.; Joseph, B. Large Scale Synthesis of Copper Nickel Alloy Nanoparticles with Reduced Compressibility Using Arc Thermal Plasma Process. Sci. Rep. 2021, 11, 7629.

(19) Vivek, S.; Preethi, S.; Kumar, T. H. V.; Sundramoorthy, A. K.; Babu, K. S. Oxidation Studies on Mono (Cu, Ni) and Bimetallic (Cu−Ni) Nanoparticles and Its Impact on Catalytic Activity. *J. Alloys Compd.* **2020**, *816*, 152608.

(20) Muntean, A.; Wagner, M.; Meyer, J.; Seipenbusch, M. Generation of Copper, Nickel, and CuNi Alloy Nanoparticles by Spark Discharge. *J. Nanopartt. Res.* **2016**, *18*, 229.

(21) Best, R. J.; Russell, W. W. Nickel, Copper and Some of Their Alloys as Catalysts for Ethylene Hydrogenation1. *J. Am. Chem. Soc.* **1954**, *76*, 838−842.

(22) Xin, H.; Niu, K.; Alsem, D. H.; Zheng, H. In Situ TEM Study of Catalytic Nanoparticle Reactions in Atmospheric Pressure Gas Environment. *Microsc. Microanal.* **2013**, *19*, 1558−1568.

(23) Hart, J. L.; Hantanasirisakul, K.; Lang, A. C.; Li, Y.; Mehmood, F.; Pachter, R.; Frenkel, A. I.; Gogotsi, Y.; Taheri, M. L. Multimodal Spectroscopic Study of Surface Termination Evolution in $Cr_2TiC_2T_x$ MXene. *Adv. Mater. Interfaces* **2021**, *8*, 2001789.

(24) Liu, D.; Li, Y.; Kottwitz, M.; Yan, B.; Yao, S.; Gamalski, A.; Grolimund, D.; Safonova, O. V.; Nachtegaal, M.; Chen, J. G.; et al. Identifying Dynamic Structural Changes of Active Sites in Pt−Ni Bimetallic Catalysts Using Multimodal Approaches. *ACS Catal.* **2018**, *8*, 4120−4131.

(25) Li, L.; Wang, L. L.; Johnson, D. D.; Zhang, Z.; Sanchez, S. I.; Kang, J. H.; Nuzzo, R. G.; Wang, Q.; Frenkel, A. I.; Li, J.; et al. Noncrystalline-to-Crystalline Transformations in Pt Nanoparticles. *J. Am. Chem. Soc.* **2013**, *135*, 13062−13072.

(26) Zhao, S.; Li, Y.; Stavitski, E.; Tappero, R.; Crowley, S.; Castaldi, M. J.; Zakharov, D. N.; Nuzzo, R. G.; Frenkel, A. I.; Stach, E. A. Operando Characterization of Catalysts through Use of a Portable Microreactor. *ChemCatChem.* **2015**, *7*, 3683−3691.

(27) Lin, S. C.; Chang, C. C.; Chiu, S. Y.; Pai, H. T.; Liao, T. Y.; Hsu, C. S.; Chiang, W. H.; Tsai, M. K.; Chen, H. M. Operando Time-Resolved X-Ray Absorption Spectroscopy Reveals the Chemical Nature Enabling Highly Selective CO_2 Reduction. *Nat. Commun.* **2020**, *11*, 3525.

(28) Gambino, M.; Veselý, M.; Filez, M.; Oord, R.; Ferreira Sanchez, D.; Grolimund, D.; Nesterenko, N.; Minoux, D.; Maquet, M.; Meirer, F.; et al. Nickel Poisoning of a Cracking Catalyst Unravelled by Single-Particle X-Ray Fluorescence-Diffraction-Absorption Tomography. *Angew. Chemie - Int. Ed.* **2020**, *59*, 3922−3927.

(29) Van Meel, K.; Smekens, A.; Behets, M.; Kazandjian, P.; Van Grieken, R. Determination of Platinum, Palladium, and Rhodium in Automotive Catalysts Using High-Energy Secondary Target X-Ray Fluorescence Spectrometry. *Anal. Chem.* **2007**, *79*, 6383−6389.

(30) Wang, Y.; Huang, M. R. S.; Salzberger, U.; Hahn, K.; Sigle, W.; van Aken, P. A. Towards Atomically Resolved EELS Elemental and Fine Structure Mapping via Multi-Frame and Energy-Offset Correction Spectroscopy. *Ultramicroscopy* **2018**, *184*, 98−105.

(31) Gloter, A.; Badjeck, V.; Bocher, L.; Brun, N.; March, K.; Marinova, M.; Tencé, M.; Walls, M.; Zobelli, A.; Stéphan, O.; et al. Atomically Resolved Mapping of EELS Fine Structures. *Mater. Sci. Semicond. Process.* **2017**, *65*, 2−17.

(32) Goulas, K. A.; Lee, J. D.; Zheng, W.; Lym, J.; Yao, S.; Oh, D. S.; Wang, C.; Gorte, R. J.; Chen, J. G.; Murray, C. B.; et al. Spectroscopic Characterization of a Highly Selective $NiCu_3$/C Hydrodeoxygenation Catalyst. *Catal. Sci. Technol.* **2018**, *8*, 6100−6108.

(33) Sadasivan, S.; Bellabarba, R. M.; Tooze, R. P. Size Dependent Reduction-Oxidation-Reduction Behaviour of Cobalt Oxide Nano-crystals. *Nanos* **2013**, *5*, 11139−11146.

(34) Sutter, E. A.; Tong, X.; Jungjohann, K.; Sutter, P. W. Oxidation of Nanoscale Au−In Alloy Particles as a Possible Route toward Stable Au-Based Catalysts. *Proc. Natl. Acad. Sci. U. S. A.* **2013**, *110*, 10519−10524.

(35) Nilsson, S.; Albinsson, D.; Antosiewicz, T. J.; Fritzsche, J.; Langhammer, C. Resolving Single Cu Nanoparticle Oxidation and Kirkendall Void Formation with in Situ Plasmonic Nanospectroscopy and Electrodynamic Simulations. *Nanoscale* **2019**, *11*, 20725−20733.

(36) Albinsson, D.; Nilsson, S.; Antosiewicz, T. J.; Zhdanov, V. P.; Langhammer, C. Heterodimers for in Situ Plasmonic Spectroscopy: Cu

Nanoparticle Oxidation Kinetics, Kirkendall Effect, and Compensation in the Arrhenius Parameters. *J. Phys. Chem. C* **2019**, *123*, 6284−6293.

(37) Peng, P.; Lin, X.-M.; Liu, Y.; Filatov, A. S.; Li, D.; Stamenkovic, V. R.; Yang, D.; Prakapenka, V. B.; Lei, A.; Shevchenko, E. V. Binary Transition-Metal Oxide Hollow Nanoparticles for Oxygen Evolution Reaction. *ACS Appl. Mater. Interfaces* **2018**, *10*, 24715−24724.

(38) Ghavamian, A.; Maghami, M. R.; Dehghan, S.; Gomes, C. Concerns of Corrosive Effects with Respect to Lightning Protection Systems. *Eng. Fail. Anal.* **2015**, *57*, 434−443.

(39) Seemala, B.; Cai, C. M.; Wyman, C. E.; Christopher, P. Support Induced Control of Surface Composition in Cu−Ni/TiO_2 Catalysts Enables High Yield Co-Conversion of HMF and Furfural to Methylated Furans. *ACS Catal.* **2017**, *7*, 4070−4082.

(40) Luo, J.; Lee, J. D.; Yun, H.; Wang, C.; Monai, M.; Murray, C. B.; Fornasiero, P.; Gorte, R. J. Base Metal-Pt Alloys: A General Route to High Selectivity and Stability in the Production of Biofuels from HMF. *Appl. Catal. B Environ.* **2016**, *199*, 439−446.

(41) Xiong, K.; Wan, W.; Chen, J. G. Reaction Pathways of Furfural, Furfuryl Alcohol and 2-Methylfuran on Cu(111) and NiCu Bimetallic Surfaces. *Surf. Sci.* **2016**, *652*, 91−97.

(42) Mironenko, A. V.; Vlachos, D. G. Conjugation-Driven "Reverse Mars−van Krevelen"-Type Radical Mechanism for Low-Temperature C−O Bond Activation. *J. Am. Chem. Soc.* **2016**, *138*, 8104−8113.

(43) Chen, L.; Liu, W.; Feng, H.; Ren, Y.; Chen, C.; Wang, S.; Yin, P.; Yang, Y.; Zhang, X.; Wei, M. Oxygen Binding Energy of Doped Metal: A Shortcut to Efficient Ni-Based Bimetallic Catalysts for the Hydrodeoxygenation Reaction. *Catal. Sci. Technol.* **2021**, *11*, 4376−4386.

(44) Sitthisa, S.; An, W.; Resasco, D. E. Selective Conversion of Furfural to Methylfuran over Silica-Supported NiAFe Bimetallic Catalysts. *J. Catal.* **2011**, *284*, 90−101.

(45) Filie, A.; Shirman, T.; Foucher, A. C.; Stach, E. A.; Aizenberg, M.; Aizenberg, J.; Friend, C. M.; Madix, R. J. Dilute Pd-in-Au Alloy RCT-SiO_2 Catalysts for Enhanced Oxidative Methanol Coupling. *J. Catal.* **2021**, *404*, 943−953.

(46) Bertella, F.; Lopes, C. W.; Foucher, A. C.; Agostini, G.; Concepción, P. C.; Stach, E. A.; Martínez, A. Insights into the Promotion with Ru of Co/TiO_2 Fischer−Tropsch Catalysts: An In Situ Spectroscopic Study. *ACS Catal.* **2020**, *10*, 6042−6057.

(47) Wang, D.; Xin, H. L.; Yu, Y.; Wang, H.; Rus, E.; Muller, D. A.; Abruña, H. D. Pt-Decorated PdCo@Pd/C Core-Shell Nanoparticles with Enhanced Stability and Electrocatalytic Activity for the Oxygen Reduction Reaction. *J. Am. Chem. Soc.* **2010**, *132*, 17664−17666.

(48) van der Hoeven, J. E. S.; Jelic, J.; Olthof, L. A.; Totarella, G.; van Dijk-Moes, R. J. A.; Krafft, J. M.; Louis, C.; Studt, F.; van Blaaderen, A.; de Jongh, P. E. Unlocking Synergy in Bimetallic Catalysts by Core−Shell Design. *Nat. Mater.* **2021**, *20*, 1216−1220.

(49) Rogatis, L. De; Montini, T.; Lorenzut, B.; Fornasiero, P. Ni_xCu_y/Al_2O_3 Based Catalysts for Hydrogen Production. *Energy Environ. Sci.* **2008**, *1*, 501−509.